gibco

24 days
of stem cells

Shape the future of stem cell innovation
October 1- November 1, 2019

Join us for 24 Days of Stem Cells; a premiere virtual event featuring the latest advances in stem cell research.

This year's format will feature a new hour of cutting edge content every week day starting October 1st. Attend the sessions that are most relevant to your work - at your convenience and at your pace.

During the 24-day long event, you can:

- Access leading scientific presentations from thought leaders around the world
- Watch live training demonstrations from our stem cell experts
- Download key stem cell tools and resources
- Complete weekly challenges to earn points towards certification and prizes

Register today at
www.24daysofstemcells.com

ThermoFisher
SCIENTIFIC

WILEY

BRIEF REPORT

WILEY Human Mutation HGVS HUMAN GENOME VARIATION SOCIETY

Clinical and functional characterization of a novel RASopathy-causing *SHOC2* mutation associated with prenatal-onset hypertrophic cardiomyopathy

Marialetizia Motta[1*] | Antonella Giancotti[2*] | Gioia Mastromoro[3] | Balasubramanian Chandramouli[4,5] | Valentina Pinna[6] | Francesca Pantaleoni[1] | Niccolò Di Giosaffatte[6] | Stefania Petrini[7] | Tommaso Mazza[8] | Valentina D'Ambrosio[2] | Paolo Versacci[9] | Flavia Ventriglia[9] | Giovanni Chillemi[10] | Antonio Pizzuti[3] | Marco Tartaglia[1] | Alessandro De Luca[6]

[1]Genetics and Rare Diseases Research Division, Ospedale Pediatrico Bambino Gesù, IRCCS, Rome, Italy

[2]Department of Maternal and Child Health and Urologic Science, Policlinico Umberto I Hospital, "Sapienza" University, Rome, Italy

[3]Department of Experimental Medicine, "Sapienza" University, Rome, Italy

[4]Compunet, Istituto Italiano di Tecnologia, Genoa, Italy

[5]Scuola Normale Superiore, Pisa, Italy

[6]Molecular Genetics Unit, Fondazione Casa Sollievo della Sofferenza, IRCCS, San Giovanni Rotondo, Italy

[7]Confocal Microscopy Core Facility, Research Laboratories, Ospedale Pediatrico Bambino Gesù, IRCCS, Rome, Italy

[8]Bioinformatics Unit, Fondazione Casa Sollievo della Sofferenza, IRCCS, San Giovanni Rotondo, Italy

[9]Department of Pediatrics, Università Sapienza, Rome, Italy

[10]DIBAF, Università della Tuscia, Viterbo, Italy

Correspondence
Marco Tartaglia, Research Division of Genetics and Rare Diseases, Ospedale Pediatrico Bambino Gesù, IRCCS, Viale di San Paolo 15, 00146 Rome, Italy.
Email: marco.tartaglia@opbg.net
Alessandro De Luca, Istituto CSS-Mendel, Viale Regina Margherita 261, 00198 Rome, Italy.
Email: a.deluca@css-mendel.it

Abstract

SHOC2 is a scaffold protein mediating RAS-promoted activation of mitogen-activated protein kinase (MAPK) signaling in response to extracellular stimuli. A recurrent activating mutation in SHOC2 (p.Ser2Gly) causes Mazzanti syndrome, a RASopathy characterized by features resembling Noonan syndrome and distinctive ectodermal abnormalities. A second mutation (p.Met173Ile) supposed to cause loss-of-function was more recently identified in two individuals with milder phenotypes. Here, we report on the third RASopathy-causing *SHOC2* mutation (c.807_808delinsTT, p.Gln269_His270delinsHisTyr), which was found associated with prenatal-onset hypertrophic cardiomyopathy. Structural analyses indicated a possible impact of the mutation on the relative orientation of the two SHOC2's leucine-rich repeat domains. Functional studies provided evidence of its activating role, revealing enhanced binding of the mutant protein to MRAS and PPP1CB, and increased signaling through the MAPK cascade. Differing from SHOC2^{S2G}, SHOC2$^{Q269\_H270delinsHY}$ is not constitutively targeted to the plasma membrane. These data document that diverse mechanisms in SHOC2 functional dysregulation converge toward MAPK signaling upregulation.

The RAS-mitogen-activated protein kinase (RAS-MAPK) signaling pathway participates in early and late developmental processes (e.g., organogenesis, morphology determination, synaptic plasticity, and growth), and dysregulation of this signaling cascade underlies the RASopathies, a group of clinically related genetic diseases affecting development and growth (Aoki, Niihori, Inoue, & Matsubara, 2016; Roberts, Allanson, Tartaglia, & Gelb, 2013; Tartaglia, Gelb, & Zenker, 2011). In these disorders, germline mutations in genes encoding RAS proteins, components of the MAPK cascade, or modulators of signal traffic through this pathway are observed (Motta et al., 2018; Simanshu, Nissley, & McCormick, 2017; Tajan, Paccoud, Branka, Edouard, & Yart, 2018; Tartaglia & Gelb, 2010), even though the relevance of signal flow perturbation involving other pathways is also emerging (Martinelli et al., 2018; Meyer Zum Büschenfelde et al., 2018). Noonan syndrome (NS; MIM #163950) represents the most common RASopathy and one of the most frequent nonchromosomal developmental disorders, with a quoted incidence of 1:2,500 live births. Major clinical features include a distinctive facial gestalt (i.e., hypertelorism, down-slanting palpebral fissures, ocular ptosis, broad forehead, and low-set ears), a variable spectrum of heart defects (pulmonary valve stenosis and hypertrophic cardiomyopathy [HCM], most commonly), postnatal reduced growth, broad/webbed neck, and chest deformities (Roberts et al., 2013). Additional frequent findings are lymphatic anomalies, cryptorchidism, bleeding diathesis, and variable developmental delay/intellectual disability (DD/ID). The wide clinical variability of NS is accounted, in part, by its genetic heterogeneity. Heterozygous gain-of-function mutations in *PTPN11* (MIM #176876) account for approximately half of NS cases (Tartaglia et al., 2001, 2002). The genes coding for the Ras guanine nucleotide exchange factor, *SOS1* (MIM #182530), serine/threonine kinase, *RAF1* (MIM #164760), small monomeric GTPase, *RIT1* (MIM #609591), and the CLR3 substrate adapter, *LZTR1* (MIM #600574), are other frequently mutated genes in NS (Aoki et al., 2013; Johnston et al., 2018; Pandit et al., 2007; Razzaque et al., 2007; Tartaglia et al., 2007; Yamamoto et al., 2015).

There is an increasing number of emerging conditions that are closely clinically related to NS. Among these, Mazzanti syndrome, also known as NS-like disorder with loose anagen hair (MIM #607721 and 617506), was first identified as caused by an invariant mutation (c.4A>G; p.Ser2Gly) in *SHOC2* (MIM #602775) (Cordeddu et al., 2009). *SHOC2* encodes a protein that consists almost entirely of leucine-rich repeats (LRRs), which are tandemly arranged to constitute a domain implicated in protein–protein interactions. The protein is a positive modulator of the RAS-MAPK signaling pathway, and functions by mediating membrane translocation of the catalytic subunit(s) of protein phosphatase 1 (PP1C), which is a required step for proper RAF1 binding to RAS and activation. Consistently, a narrow spectrum of missense mutations in *PPP1CB* (MIM #600590), one of the three paralogs encoding PP1C, has more recently been reported to underlie the disorder (Gripp et al., 2016). We originally showed that the p.Ser2Gly change in SHOC2 creates an N-myristoylation site, resulting in constitutive targeting of the mutated protein to the plasma membrane and enhanced signaling through the MAPK cascade (Cordeddu et al., 2009). Cardinal features of Mazzanti syndrome include facial characteristics resembling NS, short stature, often associated with proven growth hormone deficiency, a distinctive hyperactive behavior, darkly pigmented skin, ectodermal anomalies, including easily pluckable, sparse, thin slow-growing hair (i.e., loose anagen hair), eczema and ichthyosis, an hypernasal voice, and congenital heart defects with an over-representation of mitral valve dysplasia and septal defects. Overall, the clinical features appear more severe than those generally observed in NS during the neonatal period and infancy, even though the phenotype generally improves with age (Baldassarre et al., 2014; Cordeddu et al., 2009; Garavelli et al., 2015; Mazzanti et al., 2003). Thus far, only another pathogenic missense change has been reported to affect *SHOC2*, c.519G>A (p.Met173Ile). This variant has been reported to be associated to a mild NS-like RASopathy with clinical features partially overlapping those occurring in NS and cardiofaciocutaneous syndrome (CFCS; MIM #115150), presenting with macrocephaly, ptosis, sparse and slow-growing hair, speech delay, and hyperactive behavior (Hannig, Jeoung, Jang, Phillips, & Galperin, 2014). Unexpectedly, the mutation was reported to have loss-of-function consequences.

Here, we report on the identification and clinical and functional characterization of the third RASopathy-causing *SHOC2* mutation. Our data provide evidence of a gain-of-function role of the mutation in perturbing signaling through the MAPK cascade and document that it promotes an increased binding of SHOC2 to MRAS and PP1C, which is however uncoupled to constitutive plasma membrane targeting.

A 27-year-old Caucasian woman, gravida 1, para 0, at 23 weeks, and 5 days of gestation was referred to perform fetal echocardio-graphy due to a 4.7-mm cystic hygroma detected in first-trimester ultrasound. The woman's past obstetrical, medical, and family history was unremarkable. Serologic tests for cytomegalovirus, toxoplasmo-sis, and rubella were negative, and no exposure to teratogenic agents (i.e., ethanol abuse, smoking, and drugs) was recorded. The partner did not reveal any pathology of note and there was no consanguinity. Chorionic villus sample revealed a normal male karyotype (46,XY). The array comparative genomic hybridization (array-CGH) analysis excluded the occurrence of microdeletions and duplications. No fetal anomalies were noted during the second-trimester ultrasound screening. At fetal echocardiography (22 weeks of gestation), neither
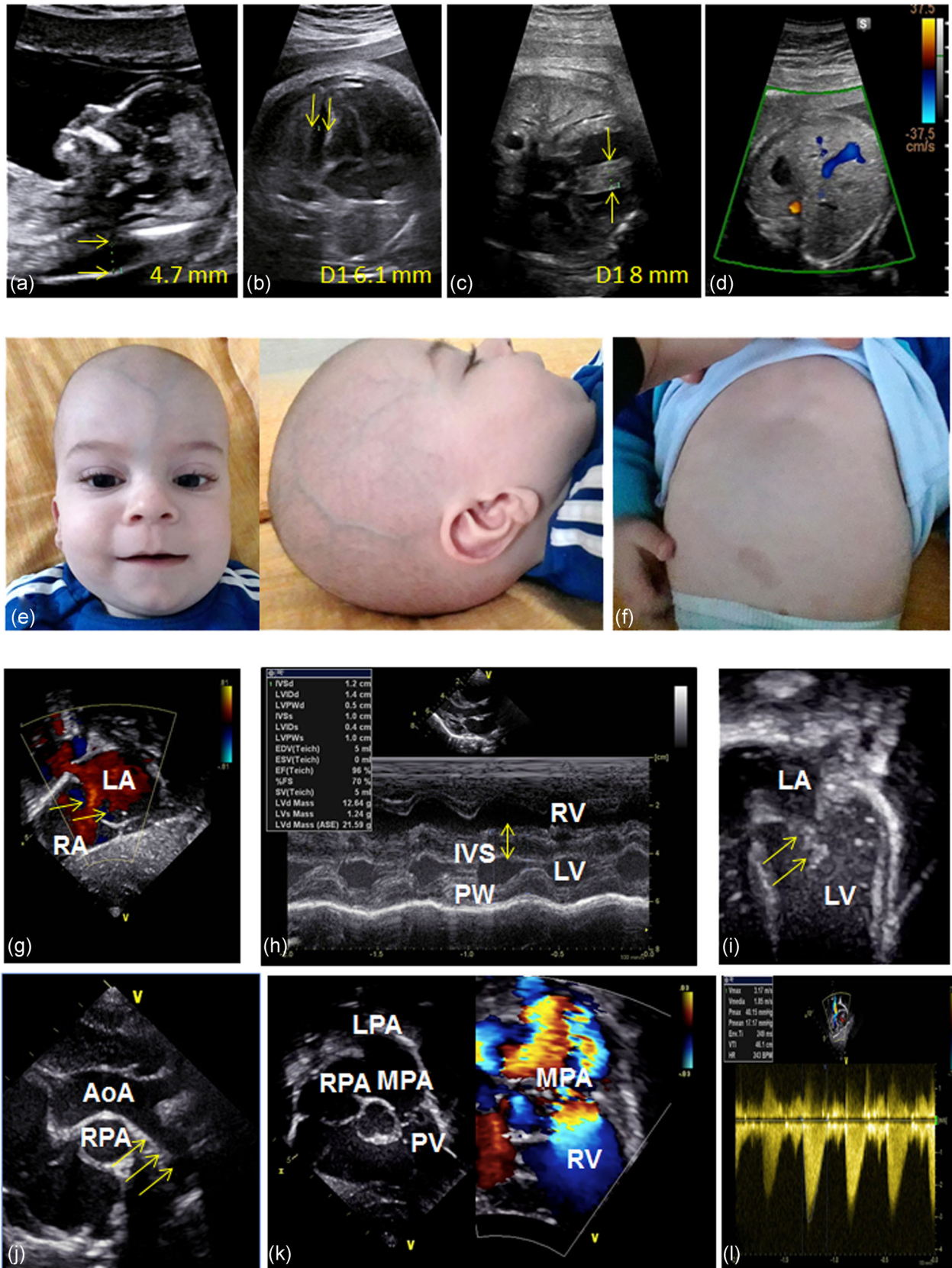
FIGURE 1   Continued.

intracardiac nor extracardiac structural anomalies were detected, but ductus venosus flow could not be assessed sonographically. The umbilical vein drained directly into the iliac vein, without an intrahepatic course. At 25 weeks, the fetus had a borderline high-interventricular septum thickness and the Doppler speed in the aortic valve was increased, with a velocity peak of 1.2 m/s. Subsequent pregnancy consultations were uneventful except for subclinical hypothyroidism managed with thyroid hormone replacement therapy. At 33 weeks of gestation, during follow-up third-trimester ultrasound, pericardial effusion was noted with no other sign of fetal anomalies, nor hydrops. Amniotic fluid was present in adequate quantity. Fetal echocardiography showed a hypertrophic interventricular septum (8 mm, >95th percentile for gestational age), mitral leaflet septal contact, redundant interatrial septum, increased aortic velocity peak up to 1.5 m/s, and mild pericardial effusion. Obstructive HCM was diagnosed. Considering the association of cystic hygroma, HCM, normal karyotype, and array-CGH assessment, targeted sequencing of a comprehensive RASopathy gene panel was performed (see below). A follow-up scan at 36 weeks of gestation showed a further increase of the interventricular septal thickness (10 mm), whereas the Doppler revealed an increased flow velocity across the aortic valve (1.8 m/s with a gradient of 15 mmHg). Fetal ultrasound images at different gestational ages are reported in Figure 1a–d. At 36 weeks of gestation, a 3,050 g male was born by emergency cesarean section for premature rupture of amniotic membranes and clinical sign of chorioamnionitis. Apgar score was 7 at 1 min and 9 at 5 min. At birth, the infant was hemodynamically stable. He presented dysmorphic features, including protruding ears and prominent lobules with two pits, short broad nose with depressed root, and long and smooth philtrum. The hair was sparse and thin. He presented chest anomalies, a single abdominal cafè-au-lait spot, and hypospadias. He was managed with intravenous fluid therapy and antibiotics for 5 days for the suspicion of maternal chorioamnionitis. Calcium gluconate supplementation for 6 days was necessary due to hypocalcemia. Transthoracic echocardiography soon after birth showed atrial septal defects, a severe asymmetric left ventricular hypertrophy with an interventricular septal diastolic

thickness of 12 mm (Z-score: + 5.54), a left ventricular posterior wall in diastole of 5 mm (Z-score: + 2.88), a systolic anterior motion of the mitral valve, which was dysplastic with redundant subvalvular apparatus and mild regurgitation, and a dysplastic pulmonary valve with diffuse thickening of the leaflets without hemodynamically significant stenosis due to still high pulmonary vascular resistance. Moreover, the aortic arch presented a mild elongation without any significant gradient. The patient was discharged at the third week of life, in a good general health state, and with indications for further outpatient treatment. The infant was revaluated at 10 and 12 months. His facial gestalt was suggestive of a RASopathy, with features including high forehead, hypertelorism, down-slanting palpebral fissures, low-set and posteriorly rotated ears, epicanthal folds, ptosis, and a short broad nose with depressed root. In addition, the infant showed long and smooth philtrum and thin lips. Poorly represented subcutaneous tissue was evident on the scalp. Hairs were sparse, thin, and slow-growing. Pectus carinatum was present in the upper two-thirds and excavatum in the lower third, and a large café-au-lait spot was present in the abdomen (Figure 1e,f). During the follow-up, the infant developed moderate pulmonary valve stenosis with a Doppler estimated peak and mean gradients across the valve of 40 mmHg and 18 mmHg, respectively, at 3 months, and 35 mmHg and 15 mmHg, at 10 months. There was also a moderate post stenotic dilation of the main pulmonary artery and of right and left pulmonary arteries. Remarkably, the follow-up heart scans showed a progressive reduction of the interventricular septal diastolic thickness up to 8 mm without subaortic significant obstruction. Transthoracic echocardiography images of the infant at birth and 3 months of life are reported in Figure 1g–l.

Molecular analysis was performed on genomic DNA isolated from amniotic fluid cells by parallel sequencing, using a panel including 16 RASopathy-related genes (*BRAF*, *CBL*, *HRAS*, *KRAS*, *LZTR1*, *MAP2K1*, *MAP2K2*, *NRAS*, *PPP1CB*, *PTPN11*, *RAF1*, *RIT1*, *RRAS*, *SHOC2*, *SOS1*, and *SOS2*; Supporting Information Material). The analysis allowed to identify a heterozygous variant in *SHOC2* (c.807_808delinsTT, p.Gln269_His270delinsHisTyr; NM_007373.3; Figure S1, panel a). The variant was validated by bidirectional Sanger

FIGURE 1 Prenatal ultrasound images, and postnatal features and echocardiography findings associated with the de novo c.807_808delinsTT change (p.Gln269_His270delinsHisTyr) in *SHOC2*. (a) Two-dimensional sonogram showing cystic hygroma (arrows), mid-sagittal view in first-trimester ultrasound. (b) Two-dimensional sonogram at 33 weeks showing mild pericardial effusion (arrows). (c) Fetal echocardiography at 33 weeks documenting a thickening of the interventricular septum (arrows). (d) Color flow map of the fetal portal circulation in an axial view. The ductus venosus could not be demonstrated. (e) Picture of the infant (10 months) showing high forehead, hypertelorism, down-slanting palpebral fissures, epicantal folds, ptosis, and low-set and posteriorly rotated ears. (f) Thorax showing pectus carinatum in the upper two-thirds and excavatum in the lower third. In the abdomen, the infant presents with a large cafè-au-lait spot. (g) Two-dimensional echocardiography at birth. The subxiphoid short-axis view shows the multiple atrial septal defects with moderate left-to-right shunt (arrows). (h) M-mode echocardiogram (parasternal long-axis views) showing hypertrophic cardiomyopathy with severe hypertrophy of the interventricular septum (12 mm) (arrow). (i) Four-chamber view showing a dysplastic mitral valve with thickened leaflets and redundant subvalvular apparatus (arrows). (j) Suprasternal notch view showing the elongation of the aortic arch (arrows). (k) Two-dimensional echocardiography at 3 months (subcostal short-axis view) showing a dysplastic pulmonary valve with thick leaflets and a moderate dilation of the main pulmonary artery and of the proximal pulmonary arteries. The color Doppler flow shows moderate turbulence through the stenotic pulmonary valve. (l) Continuous wave Doppler showing an increased flow velocity with a peak gradient of 40 mmHg and a medium gradient of about 17 mmHg. AoA: aortic arch; IVS: interventricular septum; LA: left atrium; LPA: left pulmonary artery; LV: left ventricle; MPA: main pulmonary artery; PV: pulmonary valve; PW: posterior wall; RA: right atrium; RPA: right pulmonary artery; RV: right ventricle
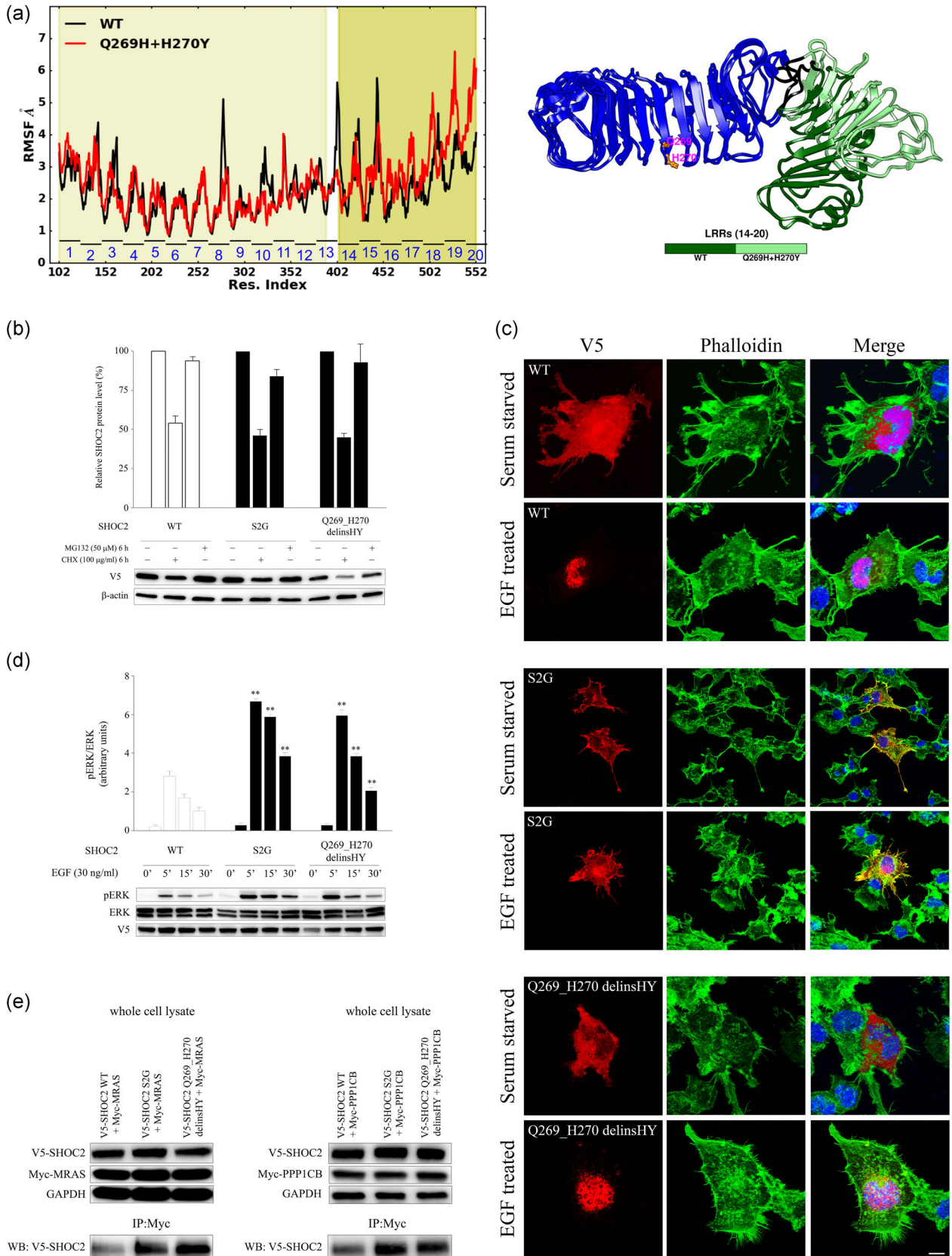
FIGURE 2 Continued.

sequencing, which also demonstrated its de novo origin (Figure S1, panel b). STR analysis confirmed paternity. The c.807_808delinsTT change had not previously been reported in public (ExAC, gnomAD, 1000 Genomes Project, and NSEuroNet) and in-house RASopathy-dedicated variant database including more than 1,000 families. The variant was submitted to the NSEuroNet (https://nseuronet.com/php/) and LOVD (http://www.lovd.nl) databases. At the protein level, this variant was predicted to result in the substitution of two adjacent amino acid residues (Gln[269]His[270]) by the HisTyr dipeptide. Both Gln[269]and His[270] are highly conserved among SHOC2 orthologs (Figure S2). In silico splicing prediction programs (SpliceSiteFinder-like, MaxEntScan, NNSPLICE [Alamut version 2.11, Interactive Biosoftware, Rouen, France]) excluded any putative consequence of the c.807_808delinsTT variant on SHOC2 transcript processing (Table S1).

SHOC2 is characterized by two distinct regions that mediate protein–protein interaction. At the N-terminus, a low-complexity and highly charged stretch (residues 7–56) contains multiple KEKE motifs that have been proposed to represent association domains or polar zippers. The second region, which encompasses most of the SHOC2's sequence (residues 102–564), includes 20 LRR motifs organized into two structurally and functionally independent domains (Motta et al., 2016), which are known to serve as a versatile module-mediating protein binding. Gln[269]His[270] are located within the conserved region of LRR 8, within the N-terminal LRR domain of the protein (Motta et al., 2016; Figure S3). Since a previous report suggested a loss-of-function effect for the only amino acid substitution within the LRR region of SHOC2 identified so far (Hannig et al., 2014), we used the previously generated homology model of the SHOC2's tandemly arranged LRR domains to explore the possible disruptive impact of the disease-causing mutation on the structural organization of LRRs 1–20. Molecular dynamics (MD) simulations (400 ns; Supporting Information Material) documented increased root mean square deviation (RMSD) values in the mutant (Gln[269]His[270]) LRR structure compared to what was observed for the wild-type (WT) structure (Figure S4), indicating the occurrence of different structural rearrangements in the two proteins. However, the time evolution of the secondary structure content did not reveal any dramatic conformational rearrangement in the mutant (Figure S5), and no major short-range perturbations of the structure (Figure S6). The protein flexibility, examined via the per-residue averaged root mean square fluctuations (RMSF), suggested a relatively more stable/rigid structural organization of the N-terminal LRR domain in the variant region of LRR motifs 8 and 10 (Figure 2a, left panel). Of note, fluctuations did not differ significantly between models within the conserved regions of LRR 8, where the mutated residues are located. A significant reduction of fluctuations was also observed in the variable region of LRR 13 (Figure 2a, left panel), which constitutes the hinge region between the two LRR domains (Motta et al., 2016). On the contrary, an increase in flexibility was observed in the C-terminal LRR domain, particularly from LRR 17 onward (Figure 2a, left panel). Box-plot representations of the average RMSF in the two LRR domains, used to provide an overall measure of the per-residue RMSF distributions, did not show significant differences between models in the N-terminal LRR domain, whereas documented higher average and maximum values in the C-terminal domain of the mutated system (Figure S7). To further characterize the structural and dynamic modifications in the His[269]Tyr[270] LRR 1–20 model, two average vectors representing the β-sheets of the N- and C-terminal LRR domains were determined and used to compute the absolute value of the angle between them (Figure S8). Comparison of angle distribution between models during the simulation documented that the native and mutated systems visit two very different structural basins (with an angle between the two LRR domains around 90° and

FIGURE 2 Structural, biochemical, and functional analyses. (a) Per-residue root mean square fluctuations (RMSF) for the wild-type (WT) and Gln[269]His[270] SHOC2 LRR 1–20 systems as a function of residue number after a MD simulation of 400 ns (left panel), and three-dimensional average structure for WT and Gln[269]His[270] SHOC2 LRR 1–20 systems (right panel). The two different backgrounds in the left panel highlight the structurally and functionally distinct LRR domains. LRR numbering is also reported (blue). Note that the variant region of LRR 20 has been removed from the analysis for its extreme flexibility. In the right panel, the N-terminal LRR domains of the two systems are superimposed, whereas the C-terminal LRR domains are represented using different tones of green. Location of Gln[269]His[270] is highlighted in orange. (b) Expression levels and stability of the SHOC2[Q269_H270delinsHY] mutant. Western blot analysis shows WT and mutant V5-tagged SHOC2 protein levels in transfected COS-1 cells, basally and after CHX (100 μg/ml) or MG132 (50 μM) treatment. Representative blots (below) and mean ± *SD* densitometry values (above) of three independent experiments are shown. β-actin was used as a loading control. (c) Subcellular localization of transiently expressed V5-tagged WT or mutated SHOC2 proteins in COS-1 cells during starvation or following EGF stimulation revealed by confocal microscopy analysis. Cells were stained with an anti-V5 monoclonal antibody and Alexa Fluor 594 goat anti-mouse secondary antibody (red). Alexa Fluor 488 phalloidin dye was used to stain the cortical actin associated with the plasma membrane (green). Nuclei are DAPI stained (blue). Merged images are shown in the right panels. Scale bar, 10 μM. (d) Overexpression of SHOC2[Q269_H270delinsHY] promoted enhanced ERK phosphorylation, as assessed by time-course experiments. Representative blots (below) and mean ± *SD* densitometry values (above) of three independent experiments are shown. Neuro2A cells were transiently transfected with the V5-tagged SHOC2 constructs, serum starved and treated with 30 ng/ml EGF for 5, 15, 30 min, or left unstimulated. Equal amounts of cell lysates were resolved on 10% polyacrylamide gel. Asterisks indicate statistically significant differences compared with WT SHOC2 at the corresponding time upon EGF stimulation (**$p < 0.01$; Student's *t* test). (e) Noonan syndrome-causing *SHOC2* mutations enhance binding of SHOC2 with MRAS (left panel) and PPP1CB (right panel). Lysates from Neuro2A cells transiently transfected to express WT and mutant V5-tagged SHOC2 proteins with Myc-MRAS or Myc-PPP1CB were immunoprecipitated with an anti-Myc antibody and assayed by western blot analysis using the indicated antibodies. CHX: cycloheximide; DAPI: 4′,6-diamidino-2-phenylindole; EGF: epidermal growth factor; ERK: extracellular signal-regulated kinase; GAPDH: glyceraldehyde 3-phosphate dehydrogenase; LRR: leucine-rich repeat; *SD*: standard deviation

45° for the WT and mutant LRRs 1–20, respectively). The different orientation of the N- versus the C-terminal LRR domain is also highlighted by the three-dimensional representation of the average MD structure generated by superimposing the N-terminal LRR domain in the two systems (Figure 2a, right panel). Overall, these data did not support any obvious disruptive effect of the mutation on the structural organization of the N-terminal LRR domain and point to a specific structural rearrangement of the protein altering the relative orientation of the two LRR domains.

To characterize the functional impact of the mutation, we introduced the Gln269_His270delinsHisTyr change in a V5-tagged SHOC2 construct cloned into the pcDNA6.2/V5-HisA eukaryotic expression vector by site-directed mutagenesis. Transient transfection experiments were performed to assess the stability and subcellular localization of the SHOC2 mutant, as well as to explore the impact of its expression on MAPK signaling (Supporting Information Material). COS-1 cells cultured in Dulbecco's modified Eagle medium supplemented with 10% heat-inactivated fetal bovine serum, and expressing WT SHOC2, SHOC2$^{Q269\_H270delinsHY}$, or the recurrent Mazzanti syndrome-causing SHOC2^{S2G} mutant were first treated with the protein-synthesis inhibitor cycloheximide or the proteasome inhibitor MG132. Consistent with the structural data, immunoblotting and relative quantitative analyses documented that the levels of the SHOC2$^{Q269\_H270delinsHY}$ mutant were similar to those characterizing the WT protein and SHOC2^{S2G} mutant (Figure 2b), indicating that the Gln269_His270delinsHisTyr change does not impact significantly the stability of the protein. We previously demonstrated that p.Ser2Gly substitution underlying the vast majority of cases with Mazzanti syndrome promotes SHOC2-constitutive targeting of the protein to the plasma membrane (Cordeddu et al., 2009). Differently from the disease-causing SHOC2^{S2G} protein, WT SHOC2 is uniformly distributed in the cytoplasm and nucleus under serum-starved condition, and translocates to the nucleus following the epidermal growth factor (EGF) stimulation, indicating that the protein has only a brief, rapidly reversed localization at the plasma membrane (Cordeddu et al., 2009). Our previous work also documented that loss of LRR 1–10 results in a redistribution of the protein that is constitutively restricted to the cytoplasm (Motta et al., 2016). To assess the possibility of mislocalization of the SHOC2$^{Q269\_H270delinsHY}$ mutant, its subcellular distribution in starved and EGF-stimulated transfected COS-1 cells was determined by confocal laser scanning microscopy. Similar to what was observed for the WT protein, SHOC2$^{Q269\_H270delinsHY}$ was distributed in both cytoplasm and nucleus during starvation, and efficiently translocated to the nucleus following stimulation with EGF (30 ng/ml; Figure 2c), ruling out any gross impact of the mutation on proper SHOC2 subcellular localization.

Similar to other RASopathy-causing mutations, we previously showed that the largely invariant Mazzanti syndrome-associated SHOC2^{S2G} mutant promotes enhanced signaling through the MAPK cascade (Cordeddu et al., 2009). To verify the presence of signal dysregulation through this signaling cascade, the dynamics of the extracellular signal-regulated kinase (ERK) phosphorylation were evaluated in time-course experiments in EGF-stimulated Neuro2A cells transiently transfected to express WT SHOC2, or each of the SHOC2^{S2G} and SHOC2$^{Q269\_H270delinsHY}$ mutants (Figure 2d). In agreement with previously reported data (Cordeddu et al., 2009; Motta et al., 2016), SHOC2^{S2G} expression promoted boosted and sustained EGF-dependent ERK phosphorylation compared to what was observed in cells expressing WT SHOC2. A less sustained but significantly enhanced ERK activation was also documented for the SHOC2$^{Q269\_H270delinsHY}$ mutant, providing evidence for its activating role on MAPK signaling. Of note, SHOC2 has been demonstrated to function as a scaffold protein linking RAS proteins to downstream signal transducers by acting as a regulatory protein of PP1C (Li, Han, & Guan, 2000; Matsunaga-Udagawa et al., 2010; Rodriguez-Viciana, Oses-Prieto, Burlingame, Fried, & McCormick, 2006). Increasing lines of evidence support the view that SHOC2 promotes PP1C translocation to the membrane by binding to activated MRAS, allowing PP1C-mediated dephosphorylation of RAF1 at a major inhibitory residue, Ser259, which is a required step for catalytic activation of the kinase (Rodriguez-Viciana et al., 2006; Young et al., 2018). To explore the possibility that the Gln269_His270delinsHis-Tyr change promotes a more stable/enhanced binding of SHOC2 to MRAS, coimmunoprecipitation assays were performed using cell lysates collected from Neuro2A cells transiently coexpressing V5-tagged WT or mutant SHOC2 proteins together with Myc-tagged MRAS (Figure 2e, left panel). As shown, both SHOC2 mutants displayed an increased MRAS binding compared to what was observed for WT SHOC2, which correlated with their improved ability to activate the ERK pathway. Finally, we compared the binding of WT SHOC2 and each of the SHOC2^{S2G} and SHOC2$^{Q269\_H270delinsHY}$ mutants to PP1C. To this goal, coimmuno-precipitation assays were carried out on lysates collected from Neuro2A cells transfected to coexpress V5-tagged WT or mutant SHOC2 proteins together with Myc-tagged PPP1CB (Figure 2e, right panel). Again, both SHOC2 mutants showed an augmented binding to the catalytic subunit of PP1 compared to WT SHOC2. Overall, the collected data support the idea that similar to what we previously demonstrated for the recurrent p.Ser2Gly change, Gln269_His270-delinsHisTyr is activating and enhances signaling through the MAPK cascade. This effect, which is attained by a still uncharacterized mechanism linked to local rearrangement of the N-terminal LRR subdomain and a more relaxed structure of the C-terminal LRR domain, is associated with an increased and/or more stable binding of SHOC2 to both MRAS and PP1C.

Here, we report on the identification of a novel RASopathy-causing SHOC2 mutation driving upregulation of MAPK signaling. Our previous work documented that a recurrent gain-of-function missense change in SHOC2 (p.Ser2Gly) causes Mazzanti syndrome (Cordeddu et al., 2009), a RASopathy characterized by an unusual combination of features, including facial anomalies suggestive of NS (and Costello syndrome [CS; MIM #218040], in the neonatal period), ectodermal anomalies, dark pigmented skin, congenital heart defects (mostly dysplasia of the mitral valve and septal defects), ID and hyperactive behavior, and reduced growth generally associated with

growth hormone deficit (Baldassarre et al., 2014; Capalbo et al., 2012; Choi et al., 2015; Cordeddu et al., 2009; Gargano et al., 2014; Gripp et al., 2013; Hoban, Roberts, Demmer, Jethva, & Shephard, 2012; Komatsuzaki et al., 2010; Lo, Wang, Wong, & Lee, 2015). More recently, a second amino acid substitution, p.Met173Ile, was reported in two individuals with a relatively mild form of RASopathy characterized by craniofacial features suggestive of NS, mild DD, hyperactive behavior, and sparse slow-growing hair, but not loose (Hannig et al., 2014). The p.Gln269_His270delinsHisTyr identified here is the third *SHOC2* mutation linked to a RASopathy phenotype. Its de novo occurrence and the functional effect of the variant on the MAPK cascade (enhanced MAPK activation), together with its associated RASopathy phenotype definitely support pathogenicity.

The clinical features associated with this mutation are within the clinical spectrum reported for Mazzanti syndrome. Features included a number of prenatal findings, such as cystic hygroma, HCM with pericardial effusion and absence of ductus venosus, and subsequent postnatal clinical assessment confirmed the distinctive facial gestalt (high forehead, hypertelorism, down-slanting palpebral fissures, and low-set and posteriorly rotated ears), and skeletal and ectodermal involvement occurring in Mazzanti syndrome. Diagnoses of RASopathies are generally made postnatally, but it may also be suspected prenatally due to abnormal ultrasound findings (Bakker, Pajkrt, Mathijssen, & Bilardo, 2011; Croonen et al., 2013; Lee et al., 2009; Nisbet, Griffin, & Chitty, 1999). Multiple structural anomalies on ultrasound imaging have been associated with other RASopathies. In NS, prenatal manifestations generally include increased nuchal translucency, cystic hygroma, polyhydramnios, cardiac anomalies, distended jugular lymphatic sacs, pleural effusion, hydrothorax, ascites, hydrops fetalis, and renal anomalies (Bakker et al., 2011; Croonen et al., 2013; Lee et al., 2009; Nisbet et al., 1999). Similarly, polyhydramnios, fetal overgrowth, relative macrocephaly and, to a lesser extent, nuchal thickening, hydrops, ventriculomegaly, pyelectasis, and fetal atrial tachycardia/arrhythmia have been reported in CS (Lin et al., 2009). Polyhydramnios, renal anomalies, lymphatic dysplasia, macrocephaly, and congenital heart defects have been observed in CFCS (Templin et al., 2016). Prenatal ultrasound abnormalities have also been observed in fetuses with Mazzanti syndrome, including polyhydramnios, increased nuchal translucency, hydrops fetalis, intrauterine growth retardation, short femurs, and congenital heart defects (i.e., ventricular septal defects and aortic coarctation; Baldassarre et al., 2014; Capalbo et al., 2012; Gargano et al., 2014; Hoban et al., 2012; Zmolikova et al., 2014). One of these babies developed HCM with left ventricular outflow tract obstruction with an unfavorable outcome at 2 months soon after birth (Hoban et al., 2012). Although this observation further emphasizes the requirement of a proper cardiological assessment of these patients, particularly during the neonatal period, the present finding highlights that the occurrence of HCM prenatally does not necessarily have negative prognostic value in the progression and severity of the disease.

Cardiovascular defects are found in the majority of individuals with RASopathy and are one of the key postnatal complications requiring medical consideration (Pierpont & Digilio, 2018). Incidence and types of cardiac anomalies differ in relation to the mutated genes and type of mutation, with well-recognized genotype–phenotype correlations (Pierpont & Digilio, 2018; Roberts et al., 2013). In patients with the *SHOC2* mutation, the most common abnormalities are cardiac septal defects (approximately 42%), pulmonary valve stenosis (approximately 40%), and mitral valve anomalies (approximately 30%; Calcagni et al., 2017, 2018; Cordeddu et al., 2009; Pierpont & Digilio, 2018). In these patients, the prevalence of HCM is estimated to be about 25%, with one-third exhibiting left ventricular outflow obstruction. Both pulmonary valve stenosis and HCM are typical examples of late-onset cardiac malformations, which may appear during the third trimester of pregnancy or after birth. In the present case, HCM was detected in the third trimester, worsened toward the end of pregnancy and after birth, but was characterized by a subsequent improvement. In RASopathies, HCM is generally characterized by important ventricular hypertrophy and increased prevalence of left ventricular outflow obstruction (Calcagni et al., 2017, 2018; Pierpont & Digilio, 2018). In this case, the follow-up serial echocardiograms documented a progressive reduction of the interventricular septal thickness without the residual obstruction of the left ventricular outflow tract. In addition to HCM and polyvalvular dysplasia, the infant was diagnosed with agenesis of ductus venosus. Although this defect is known to be associated with other syndromic disorders, it has been recurrently reported in NS (Newman, Wanner, & Brown, 2017). Of note, consistently with all previously described patients (Bradley, Kean, Twining, & James, 2001; Currarino, Stannard, & Kolni, 1991; Demirci et al., 2015; Leonidas & Fellows, 1976; Newman et al., 2017), agenesis of ductus venosus subtype occurred with direct umbilical drainage into an iliac vein, further confirming the occurrence of this specific subtype of vascular anomaly in NS and related traits.

Virtually all patients with Mazzanti syndrome carry the recurrent p.Ser2Gly mutation, which causes N-terminal myristoylation of SHOC2 and its constitutive targeting to the plasma membrane and impaired nuclear translocation following growth factor stimulation (Cordeddu et al., 2009). Both of these events are likely to contribute to enhancing signal flow through the MAPK cascade (Motta et al., 2016). Though the role of SHOC2 in the nucleus still remains elusive, the present and recent data from others consistently indicate that stable membrane binding of SHOC2 supports the interaction of the protein with MRAS, favoring membrane localization of PP1C, and RAF1 activation (Young et al., 2018). Similarly to what is observed for myristoylated SHOC2, SHOC2$^{Q269\_H270delinsHY}$ promotes enhanced ERK phosphorylation and an augmented or more stable binding to both MRAS and PP1C. As no altered subcellular localization and trafficking was documented in this mutant, at least in the used experimental conditions, it is likely that the specific behavior of this mutant is determined by local structural rearrangement of the N-terminal LRR domain and an indirect effect on the C-terminal LRR domain stabilizing the MRAS–SHOC2–PP1C complex. Of note, this model has been recently confirmed experimentally (Young et al., 2018). Differently from the p.Ser2Gly and p.Gln269_His270delinsHisTyr changes, p.Met173Ile was originally

reported to behave as a loss-of-function mutation (Hannig et al., 2014). However, recently published data (Young et al., 2018) and our observation (Tartaglia and den Hertog, unpublished) consistently support an activating role of this amino acid substitution on SHOC2 interaction with MRAS and PP1C as well as on MAPK signaling. Taken together, these data indicate that, through different mechanisms, the three identified RASopathy-causing SHOC2 variants (p.Ser2Gly, p.Met173Ile, and p.Gln269_His270delinsHisTyr) behave as gain-of-function mutations to upregulate RAS signaling through the MAPK cascade, selectively promoting SHOC2 complex formation with MRAS and PP1C.

In conclusion, we report here a novel RASopathy-causing *SHOC2* variant associated with prenatal-onset HCM. Our data document that this variant results in enhanced MRAS and PPP1CB binding and increased MAPK activation, but does not drive constitutive translocation of SHOC2 to the plasma membrane. These findings expand the molecular spectrum of *SHOC2* mutations and the complexity of the molecular mechanisms implicated in SHOC2 functional dysregulation.

CONFLICT OF INTERESTS

The authors declare that there are no conflict of interests.

ORCID

Marco Tartaglia 🅳 http://orcid.org/0000-0001-7736-9672
Alessandro Luca 🅳 http://orcid.org/0000-0002-4408-8062

REFERENCES

Aoki, Y., Niihori, T., Banjo, T., Okamoto, N., Mizuno, S., Kurosawa, K., … Matsubara, Y. (2013). Gain-of-function mutations in RIT1 cause Noonan syndrome, a RAS/MAPK pathway syndrome. *American Journal of Human Genetics*, *93*, 173–180. https://doi.org/10.1016/j.ajhg.2013.05.021

Aoki, Y., Niihori, T., Inoue, S., & Matsubara, Y. (2016). Recent advances in RASopathies. *Journal of Human Genetics*, *61*, 33–39. https://doi.org/10.1038/jhg.2015.114

Bakker, M., Pajkrt, E., Mathijssen, I. B., & Bilardo, C. M. (2011). Targeted ultrasound examination and DNA testing for Noonan syndrome, in fetuses with increased nuchal translucency and normal karyotype. *Prenatal Diagnosis*, *31*, 833–840. https://doi.org/10.1002/pd.2782

Baldassarre, G., Mussa, A., Banaudi, E., Rossi, C., Tartaglia, M., Silengo, M., & Ferrero, G. B. (2014). Phenotypic variability associated with the invariant SHOC2 c.4A>G (p.Ser2Gly) missense mutation. *American Journal of Medical Genetics. Part A*, *164A*, 3120–3125. https://doi.org/10.1002/ajmg.a.36697

Bradley, E., Kean, L., Twining, P., & James, D. (2001). Persistent right umbilical vein in a fetus with Noonan's syndrome: a case report. *Ultrasound in Obstetrics & Gynecology*, *17*, 76–78.

Calcagni, G., Limongelli, G., D'Ambrosio, A., Gesualdo, F., Digilio, M. C., Baban, A., … Marino, B. (2017). Data on cardiac defects, morbidity and mortality in patients affected by RASopathies. CARNET study results. *Data in Brief*, *16*, 649–654. https://doi.org/10.1016/j.dib.2017.11.085

Calcagni, G., Adorisio, R., Martinelli, S., Grutter, G., Baban, A., Versacci, P., … Marino, B. (2018). Clinical Presentation and Natural History of Hypertrophic Cardiomyopathy in RASopathies. *Heart Failure Clinics*, *4*, 225–235. https://doi.org/10.1016/j.hfc.2017.12.005

Capalbo, D., Scala, M. G., Melis, D., Minopoli, G., Improda, N., Palamaro, L., … Salerno, M. (2012). Clinical heterogeneity in two patients with Noonan-like syndrome associated with the same SHOC2 mutation. *Italian Journal of Pediatrics*, *38*, 48. https://doi.org/10.1186/1824-7288-38-48

Choi, J. H., Oh, M. Y., Yum, M. S., Lee, B. H., Kim, G. H., & Yoo, H. W. (2015). Moyamoya syndrome in a patient with Noonan-like syndrome with loose anagen hair. *Pediatric Neurology*, *52*, 352–355. https://doi.org/10.1016/j.pediatrneurol.2014.11.017

Corddeu, V., Di Schiavi, E., Pennacchio, L. A., Ma'ayan, A., Sarkozy, A., Fodale, V., … Tartaglia, M. (2009). Mutation of SHOC2 promotes aberrant protein N-myristoylation and causes Noonan-like syndrome with loose anagen hair. *Nature Genetics*, *41*, 1022–1026. https://doi.org/10.1038/ng.425

Croonen, E. A., Nillesen, W. M., Stuurman, K. E., Oudesluijs, G., van de Laar, I. M., Martens, L., … Yntema, H. G. (2013). Prenatal diagnostic testing of the Noonan syndrome genes in fetuses with abnormal ultrasound findings. *European Journal of Human Genetics*, *21*, 936–942. https://doi.org/10.1038/ejhg.2012.285

Currarino, G., Stannard, M. W., & Kolni, H. (1991). Umbilical vein draining into the inferior vena cava via the internal iliac vein, bypassing the liver. *Pediatric Radiology*, *21*, 265–266. PMID: 1870921

Demirci, O., Yavuz, T., Arisoy, R., Pekin, O., Acar, H., Aydin, H., … Kumru, P. (2015). Agenesis of the ductus venosus—A case with Noonan syndrome. *Genetic Counseling*, *26*, 373–376. PMID: 26625673

Garavelli, L., Cordeddu, V., Errico, S., Bertolini, P., Street, M. E., Rosato, S., … Tartaglia, M. (2015). Noonan syndrome-like disorder with loose anagen hair: A second case with neuroblastoma. *American Journal of Medical Genetics. Part A*, *167A*, 1902–1907. https://doi.org/10.1002/ajmg.a.37082

Gargano, G., Guidotti, I., Balestri, E., Vagnarelli, F., Rosato, S., Comitini, G., … Garavelli, L. (2014). Hydrops fetalis in a preterm newborn heterozygous for the c.4A>G SHOC2 mutation. *American Journal of Medical Genetics. Part A*, *164A*, 1015–1020. https://doi.org/10.1002/ajmg.a.36376

Gripp, K. W., Zand, D. J., Demmer, L., Anderson, C. E., Dobyns, W. B., Zackai, E. H., … Sol-Church, K. (2013). Expanding the SHOC2 mutation associated phenotype of Noonan syndrome with loose anagen hair: Structural brain anomalies and myelofibrosis. *American Journal of Medical Genetics. Part A*, *161A*, 2420–2430. https://doi.org/10.1002/ajmg.a.36098

Gripp, K. W., Aldinger, K. A., Bennett, J. T., Baker, L., Tusi, J., Powell-Hamilton, N., … Dobyns, W. B. (2016). A novel rasopathy caused by recurrent de novo missense mutations in PPP1CB closely resembles Noonan syndrome with loose anagen hair. *American Journal of Medical Genetics. Part A*, *170*, 2237–2247. https://doi.org/10.1002/ajmg.a.37781

Hannig, V., Jeoung, M., Jang, E. R., Phillips, J. A., 3rd, & Galperin, E. (2014). A Novel SHOC2 Variant in Rasopathy. *Human Mutation*, *35*, 1290–1294. https://doi.org/10.1002/humu.22634

Hoban, R., Roberts, A. E., Demmer, L., Jethva, R., & Shephard, B. (2012). Noonan syndrome due to a SHOC2 mutation presenting with fetal distress and fatal hypertrophic cardiomyopathy in a premature infant. *American Journal of Medical Genetics. Part A*, 158A, 1411–1413. https://doi.org/10.1002/ajmg.a.35318

Johnston, J. J., van der Smagt, J. J., Rosenfeld, J. A., Pagnamenta, A. T., Alswaid, A., Baker, E. H., … Biesecker, L. G. (2018). Autosomal recessive Noonan syndrome associated with biallelic LZTR1 variants. *Genetics in Medicine*, 20, 1175–1185. https://doi.org/10.1038/gim.2017.249

Komatsuzaki, S., Aoki, Y., Niihori, T., Okamoto, N., Hennekam, R. C., Hopman, S., … Matsubara, Y. (2010). Mutation analysis of the SHOC2 gene in Noonan-like syndrome and in hematologic malignancies. *Journal of Human Genetics*, 55, 801–809. https://doi.org/10.1038/jhg.2010.116

Lee, K. A., Williams, B., Roza, K., Ferguson, H., David, K., Eddleman, K., … Kornreich, R. (2009). PTPN11 analysis for the prenatal diagnosis of Noonan syndrome in fetuses with abnormal ultrasound findings. *Clinical Genetics*, 75, 190–194. https://doi.org/10.1111/j.1399-0004.2008.01085.x

Leonidas, J. C., & Fellows, R. A. (1976). Congenital absence of the ductus venosus: With direct connection between the umbilical vein and the distal inferior vena cava. *AJR. American Journal of Roentgenology*, 126, 892–895. https://doi.org/10.2214/ajr.126.4.892

Li, W., Han, M., & Guan, K. L. (2000). The leucine-rich repeat protein SUR-8 enhances MAP kinase activation and forms a complex with Ras and Raf. *Genes & Development*, 14, 895–900.

Lin, A. E., O'Brien, B., Demmer, L. A., Almeda, K. K., Blanco, C. L., Glasow, P. F., … Gripp, K. W. (2009). Prenatal features of Costello syndrome: Ultrasonographic findings and atrial tachycardia. *Prenatal Diagnosis*, 29, 682–690. https://doi.org/10.1002/pd.2276

Lo, F. S., Wang, C. J., Wong, M. C., & Lee, N. C. (2015). Moyamoya disease in two patients with Noonan-like syndrome with loose anagen hair. *American Journal of Medical Genetics. Part A*, 167, 1285–1288. https://doi.org/10.1002/ajmg.a.37053

Martinelli, S., Krumbach, O. H. F., Pantaleoni, F., Coppola, S., Amin, E., Pannone, L., … Mirzaa, G. M. (2018). Functional dysregulation of CDC42 causes diverse developmental phenotypes. *American Journal of Human Genetics*, 102, 309–320. https://doi.org/10.1016/j.ajhg.2017.12.015

Matsunaga-Udagawa, R., Fujita, Y., Yoshiki, S., Terai, K., Kamioka, Y., Kiyokawa, E., … Matsuda, M. (2010). The scaffold protein Shoc2/SUR-8 accelerates the interaction of Ras and Raf. *Journal of Biological Chemistry*, 285, 7818–7826. https://doi.org/10.1074/jbc.M109.053975

Mazzanti, L., Cacciari, E., Cicognani, A., Bergamaschi, R., Scarano, E., & Forabosco, A. (2003). Noonan-like syndrome with loose anagen hair: A new syndrome? *American Journal of Medical Genetics. Part A*, 118A, 279–286. https://doi.org/10.1002/ajmg.a.10923

Meyer Zum Büschenfelde, U., Brandenstein, L. I., von Elsner, L., Flato, K., Holling, T., Zenker, M., … Kutsche, K. (2018). RIT1 controls actin dynamics via complex formation with RAC1/CDC42 and PAK1. *PLOS Genetics*, 14, e1007370. https://doi.org/10.1371/journal.pgen.1007370

Motta, M., Chillemi, G., Fodale, V., Cecchetti, S., Coppola, S., Stipo, S., … Tartaglia, M. (2016). SHOC2 subcellular shuttling requires the KEKE motif-rich region and N-terminal leucine-rich repeat domain and impacts on ERK signalling. *Human Molecular Genetics*, 25, 3824–3835. https://doi.org/10.1093/hmg/ddw229

Motta, M., Fidan, M., Bellacchio, E., Pantaleoni, F., Schneider-Heieck., K., Coppola, S., … Tartaglia, M. (2018). Dominant Noonan syndrome-causing LZTR1 mutations specifically affect the kelch domain substrate-recognition surface and enhance RAS-MAPK signaling. *Human Molecular Genetics*, 28, 1007–1022. https://doi.org/10.1093/hmg/ddy412

Newman, C. L., Wanner, M. R., & Brown, B. P. (2017). Prenatal and postnatal sonographic confirmation of congenital absence of the ductus venosus in a child with Noonan syndrome. *Case Reports in Radiology*, 2017, 3068178–3. https://doi.org/10.1155/2017/3068178

Nisbet, D. L., Griffin, D. R., & Chitty, L. S. (1999). Prenatal features of Noonan syndrome. *Prenatal Diagnosis*, 19, 642–647. PMID: 10419612

Pandit, B., Sarkozy, A., Pennacchio, L. A., Carta, C., Oishi, K., Martinelli, S., … Gelb, B. D. (2007). Gain-of-function RAF1 mutations cause Noonan and LEOPARD syndromes with hypertrophic cardiomyopathy. *Nature Genetics*, 39, 1007–1012. https://doi.org/10.1038/ng2073

Pierpont, M. E., & Digilio, M. C. (2018). Cardiovascular disease in Noonan syndrome. *Current Opinion in Pediatrics*, 30, 601–608. https://doi.org/10.1097/MOP.0000000000000669

Razzaque, M. A., Nishizawa, T., Komoike, Y., Yagi, H., Furutani, M., Amo, R., … Matsuoka, R. (2007). Germline gain-of-function mutations in RAF1 cause Noonan syndrome. *Nature Genetics*, 39, 1013–1017. https://doi.org/10.1038/ng2078

Roberts, A. E., Allanson, J. E., Tartaglia, M., & Gelb, B. D. (2013). Noonan syndrome. *Lancet*, 381, 333–342. https://doi.org/10.1016/S0140-6736(12)61023-X

Rodriguez-Viciana, P., Oses-Prieto, J., Burlingame, A., Fried, M., & McCormick, F. (2006). A phosphatase holoenzyme comprised of Shoc2/Sur8 and the catalytic subunit of PP1 functions as an M-Ras effector to modulate Raf activity. *Molecular Cell*, 22, 217–230. https://doi.org/10.1016/j.molcel.2006.03.027

Simanshu, D. K., Nissley, D. V., & McCormick, F. (2017). RAS proteins and their regulators in human disease. *Cell*, 170, 17–33. https://doi.org/10.1016/j.cell.2017.06.009

Tajan, M., Paccoud, R., Branka, S., Edouard, T., & Yart, A. (2018). The RASopathy family: Consequences of germline activation of the RAS/MAPK pathway. *Endocrine Reviews*, 39, 676–700. https://doi.org/10.1210/er.2017-00232

Tartaglia, M., & Gelb, B. D. (2010). Disorders of dysregulated signal traffic through the RAS-MAPK pathway: Phenotypic spectrum and molecular mechanisms. *Annals of the New York Academy of Sciences*, 1214, 99–121. https://doi.org/10.1111/j.1749-6632.2010.05790.x

Tartaglia, M., Gelb, B. D., & Zenker, M. (2011). Noonan syndrome and clinically related disorders. *Best Practice & Research Clinical Endocrinology & Metabolism*, 25, 161–179. https://doi.org/10.1016/j.beem.2010.09.002

Tartaglia, M., Kalidas, K., Shaw, A., Song, X., Musat, D. L., van der Burgt, I., … Gelb, B. D. (2002). PTPN11 mutations in Noonan syndrome: Molecular spectrum, genotype-phenotype correlation, and phenotypic heterogeneity. *American Journal of Human Genetics*, 70, 1555–1563. https://doi.org/10.1086/340847

Tartaglia, M., Mehler, E. L., Goldberg, R., Zampino, G., Brunner, H. G., Kremer, H., … Gelb, B. D. (2001). Mutations in PTPN11, encoding the protein tyrosine phosphatase SHP-2, cause Noonan syndrome. *Nature Genetics*, 29, 465–468. https://doi.org/10.1038/ng772

Tartaglia, M., Pennacchio, L. A., Zhao, C., Yadav, K. K., Fodale, V., Sarkozy, A., … Gelb, B. D. (2007). Gain-of-function SOS1 mutations cause a distinctive form of Noonan syndrome. *Nature Genetics*, 39, 75–79. https://doi.org/10.1038/ng1939

Templin, L., Baumann, C., Busa, T., Heckenroth, H., Pouvreau, N., Toutain, A., … Philip, N. (2016). Prenatal findings in cardio-facio-cutaneous syndrome. *American Journal of Medical Genetics. Part A*, 170A, 441–445. https://doi.org/10.1002/ajmg.a.37420

Yamamoto, G. L., Aguena, M., Gos, M., Hung, C., Pilch, J., Fahiminiya, S., … Bertola, D. R. (2015). Rare variants in SOS2 and LZTR1 are associated with Noonan syndrome. *Journal of Medical Genetics*, 52, 413–421. https://doi.org/10.1136/jmedgenet-2015-103018

Young, L. C., Hartig, N., Boned Del Río, I., Sari, S., Ringham-Terry, B., Wainwright, J. R., … Rodriguez-Viciana, P. (2018). SHOC2-MRAS-PP1 complex positively regulates RAF activity and contributes to Noonan syndrome pathogenesis. *Proceedings of the National Academy of Sciences of the United States of America*, 115, E10576–E10585. https://doi.org/10.1073/pnas.1720352115

Zmolikova, M., Puchmajerova, A., Hecht, P., Lebl, J., Trkova, M., & Krepelova, A. (2014). Coarctation of the aorta in Noonan-like

syndrome with loose anagen hair. *American Journal of Medical Genetics. Part A, 164A,* 1218–1221. https://doi.org/10.1002/ajmg.a.36404

SUPPORTING INFORMATION

Additional supporting information may be found online in the Supporting Information section at the end of the article.